ACS OMEGA

Open Access

http://pubs.acs.org/journal/acsodf

Article

First-Principles Investigation of Hydroxyl Species Formation on β-MnO_2(110) for Catalytic Oxidation Applications

Bunrat Tharat, Panupol Untarabut, Anchalee Junkaew,* and Suwit Suthirakun*

Cite This: *ACS Omega* 2025, 10, 12097−12108

Read Online

ACCESS | Metrics & More | Article Recommendations | Supporting Information

ABSTRACT: Hydroxyl (OH) species play a critical role in several oxidative catalysis processes, including the oxidation of 5-hydroxymethylfurfural (HMF) to produce valuable compounds like 2,5-furandicarboxylic acid (FDCA). High OH coverage on metal oxide surfaces significantly enhanced catalytic activity. Herein, we investigated OH coverage on the β-MnO_2(110) surface generated through the decomposition of oxidant molecules (O_2, H_2O_2, and *tert*-butyl hydroperoxide, TBHP) using density functional theory (DFT) calculations and ab initio thermodynamic modeling. We studied the kinetics and thermodynamics aspects of OH formation pathways, focusing on direct O−O and C−O bond cleavages and reactions with H_2O, both in gas and solvent environments. Computations reveal that TBHP and H_2O_2 exhibit lower dissociation barriers and favorable thermodynamics than O_2, yielding higher OH coverage under relevant reaction conditions. Phase diagrams constructed from thermodynamic models reveal that TBHP maintains high OH coverage across a broader temperature range, suggesting its potential as an efficient oxidant for catalytic applications. These insights support the development of β-MnO_2 catalysts tailored for oxidation processes by guiding oxidant selection and reaction conditions.

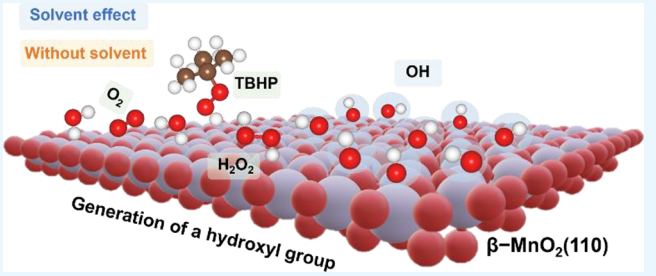

1. INTRODUCTION

Hydroxyl (OH) species are one of the most important oxidizing agents for converting lignocellulosic compounds such as 5-hydroxymethylfurfural (HMF) into valuable products such as 2,5-furandicarboxylic acid (FDCA). The surface OH acts as an active oxygen species on metal oxide catalysts and plays a crucial role in the HMF oxidation reaction. As reported in our previous work,[1] the surface OH on β-MnO_2 can promote FDCA production from HMF, which showed a high HMF conversion (≥99 mol %) and high FDCA yield (85−92 mol %) during continuous flow oxidation for 72 h at a pO_2 of 1 MPa and 393 K, with a liquid hourly space velocity (LHSV) of 1 h^{-1}. High OH coverage on the β-MnO_2 surface shows high catalytic activity for the HMF oxidation reaction. The OH radical can facilitate dehydrogenation reactions during the HMF oxidation process on transition-metal[2,3] and metal oxide catalysts.[1] In addition, it plays a vital role in abstracting a hydrogen atom from the C−H and O−H bonds of the geminal-diol intermediate structure to form a carboxylic group. Therefore, OH coverage on the catalyst surface is one of the vital factors determining the HMF oxidation reaction.

The formation of the surface OH group occurs through hydroxylation[4] or by adding an OH source, typically from a base or oxidant molecules.[5−8] For instance, in the conversion of HMF to FDCA on metal oxide catalysts, surface OH species can be generated using oxidants such as dissolved oxygen gas (O_2),[9,10] hydrogen peroxide (H_2O_2),[5−7,11] or *tert*-butyl hydroperoxide (TBHP),[8,12] providing yields greater than 85%. Among these, O_2 exhibits relatively low oxidative ability, resulting in slower reaction rates and often requiring high temperatures (≥100 °C) and pressures (≥10 bar) to achieve significant yields.[13−15] In contrast, TBHP displays higher catalytic activity for HMF oxidation on Cu-doped MnO_2 catalysts, resulting in superior HMF conversion (99.4%) and a higher FDCA yield (96.3%) compared to O_2 and H_2O_2, respectively.[8] These oxidants serve as resources to generate surface OH species, which possess a strong oxidative ability for the HMF oxidation reaction.

In general, O_2, TBHP, and H_2O_2 are used as oxidizing agents for various oxidation reactions. O_2 and H_2O_2 are widely used in various oxidation processes due to their mild nature and ability to generate reactive oxygen species under suitable conditions. However, they typically result in a rather low oxidative power. For example, the use of O_2 and H_2O_2 as oxidants results in HMF conversion of less than 57% and very low FDCA selectivity on Cu-doped MnO_2 catalysts.[8] In contrast, TBHP, a rather strong oxidant, yields high HMF conversion (>99%) and high FDCA selectivity (>96%).[8]

Received: November 11, 2024
Revised: March 6, 2025
Accepted: March 11, 2025
Published: March 18, 2025

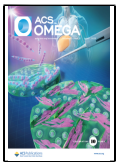

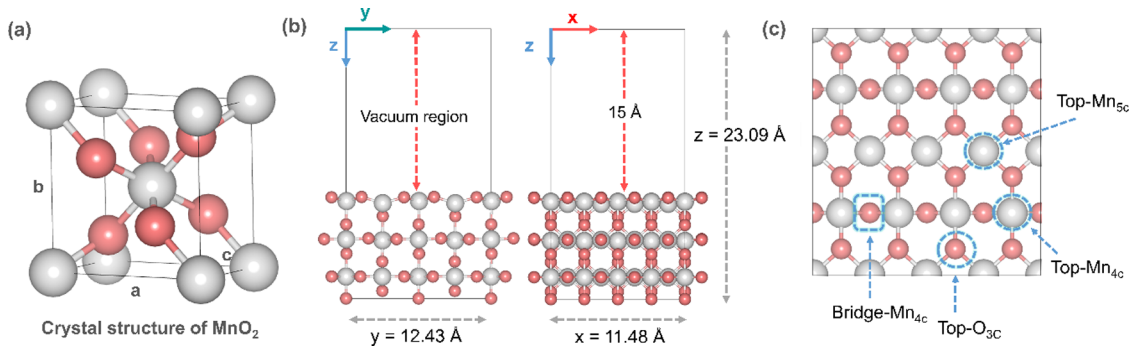

Figure 1. Schematic representation of (a) unit cell of MnO_2, (b) slab model of the β-MnO_2 (110) surface projected along the (010) direction (left); (100) direction (right); and (c) possible active sites on the β-MnO_2(110) surface. The red and gray spheres represent O and Mn atoms, respectively.

MnO_2 has been considered as a promising oxidative catalyst due to its low cost and effectiveness in the oxidation reaction. Among various crystal structures, it has been reported that β-MnO_2 is the best-performing catalyst, where the oxidation of HMF involves oxygen from the MnO_2 surface.[10,16] Also, the β-MnO_2(110) surface is the most stable low-index surface.[17−21] Moreover, it is the most easily oxidized surface,[10,22] and it shows high oxidative abilities.[10] The oxidation process facilitated by lattice oxygen species depends on the reducibility of the metal oxide catalysts, which is influenced by their oxygen vacancy formation energy.[10] Extensive experimental[10,23] and computational studies[24] have been conducted on this aspect. The literature has extensively studied OH generation from oxidant molecules on metal and metal oxide[25−27] catalysts. However, a comprehensive theoretical investigation into the coverage of the OH group from oxidant molecules on transition-metal oxide catalysts, in particular the β-MnO_2 surface, is still lacking. Understanding the formation of hydroxyl groups from the decomposition of oxidant molecules on β-MnO_2 remains limited due to the complexity of its structural diversity, mainly due to different bonding patterns of MnO_6 octahedra.[28−30] In addition to the structural diversity of MnO_2, the magnetic properties of Mn centers in the materials need to be systematically modeled.[31,32] Gaining a deeper molecular-level understanding of OH coverage on β-MnO_2 catalysts is crucial for the development and design of catalysts with high activity for the HMF oxidation reaction.

From the limited understanding of surface OH formation on β-MnO_2 catalysts, this study aims to use first-principles computations to model the thermodynamics of OH coverage on the β-MnO_2(110) surface under experimental conditions, focusing on the influence of different oxidants. In particular, we examine how OH coverage arises from the dissociation of various oxidant molecules, including O_2, H_2O_2, and TBHP. To achieve this, we first explored the adsorption behavior of oxidant molecules in the absence and presence of solvent effects using an implicit solvent model. Then, we further investigated the effects of temperature and pressure of the oxidant molecules on OH coverage and provided a relationship between experimental conditions and density functional theory (DFT) calculations within the constructed thermodynamic model. Finally, surface phase diagrams were generated by considering the surface free energies of different OH coverages and the chemical potential of the oxidant molecules. This study provides a deeper molecular-level guidance for the design of more efficient catalysts for the HMF oxidation reaction.

2. COMPUTATIONAL DETAILS

All calculations were carried out using the planewave-based density functional theory (DFT)[33] method as implemented in the Vienna ab initio simulation package (VASP 5.4.4) with a kinetic energy cutoff of 500 eV for the planewave basis.[34,35] The exchange-correlation functional was described using the Perdew−Burke−Ernzerhof functional (PBE) form of the generalized gradient approximation (GGA).[36] The projector augmented wave (PAW) method was used to describe the electron ion-core interactions.[37,38] To describe the strongly correlated d electrons of β-MnO_2, the DFT+U approach was used with Hubbard-like terms U = 2.8 eV and J = 1.2 eV for Mn 3d electrons, as suggested by Mellan et al.[19,39,40] An antiferromagnetic state was used for the β-MnO_2 model, as reported by previous works.[32,41] van der Waals interactions were applied using the DFT-D3 method proposed by Grimme et al.[42]

To construct the surface model, we first optimized the unit cell of β-MnO_2 using a 7 × 7 × 7 Monkhorst−Pack (MP)[43] k-mesh, which yielded the calculated lattice parameters of $a = b$ = 4.396 Å and c = 2.871 Å. Then, we used the optimized unit cell to build the 4 × 2 (110) slab model, with dimensions of 11.48 × 12.43 Å, containing three molecular layers of 48 Mn and 96 O atoms. A vacuum gap of 15 Å were added in the normal direction to avoid spurious interactions between its periodic images. The bottom layer was fixed to mimic the bulk lattice positions.

All adsorbed intermediates on the surface were optimized using an MP k-point grid of 2 × 2 × 1, with force and energy convergence criteria of 0.02 eV/Å and 10^{-6} eV, respectively. The climbing image nudged elastic band (CINEB)[44] and DIMER methods[45−47] were employed for finding the transition states (TS). The CINEB method requires multiple images to form a path, while the DIMER method only needs two images for searching transition states (TS). The string method, using multiple images, is time-consuming. In this work, we use the CINEB method as the main approach and apply the DIMER method to refine the TS structures. The transition state structures from both methods were confirmed through frequency calculations showing only one imaginary frequency. Conventional DFT calculations are typically performed under vacuum, while reaction pathways and adsorption processes occur in aqueous environments. This work explores the activation of oxidant molecules on the β-MnO_2(110) surface, considering the influence of solvents on reaction pathways and barriers.[48,49] To account for solvation

https://doi.org/10.1021/acsomega.4c10253
ACS Omega 2025, 10, 12097−12108

effects, we used an implicit solvation model of VASPsol[50−52] with a water dielectric constant (ε = 78.40). While the absence of explicit water solvent molecules could lead to an underestimation of specific local intermolecular interactions and structural reorganizations, the implicit solvation model provides a computationally efficient approach to include solvation effects.

3. RESULTS AND DISCUSSION

3.1. Structure of the β-MnO_2(110) Surface. The crystal structure of β-MnO_2 develops a rutile-type tetragonal structure with space group $P4/mnm$.[53,54] It is one of the most thermodynamically stable MnO_2 allotropes, formed by a single chain of edge-sharing MnO_6 octahedra.[55,56] The optimized unit cell, as shown in Figure 1a, exhibits lattice parameters of $a = b$ = 4.396 Å and c = 2.871 Å, which are within 0.07% error from the experimental values ($a = b$ = 4.398 Å, c = 2.873 Å).[57]

A 4 × 2 β-MnO_2 (110) slab was constructed using the optimized bulk unit cell, as illustrated in Figure 1b. The (110) surface of β-MnO_2 is particularly interesting due to its low surface energy,[19,57] offering various active sites that can facilitate the adsorption of oxidant molecules. Therefore, calculations for equilibrium geometries and energies were conducted by using this surface. These active sites include the atop site of four-fold Mn (top-Mn_{4c}), the atop site of five-fold Mn (top-Mn_{5c}), and the bridge site between two four-fold Mn atoms (bridge-Mn_{4c}), as shown in Figure 1c.

These active sites are characterized as Lewis acid sites[58,59] that can effectively bind to electronegative atoms, such as the oxygen atoms in oxidant molecules, making the β-MnO_2 (110) surface catalytically active for oxidation reactions. In particular, the top-Mn_{4c} site, with its lower coordination number, exhibits a higher degree of unsaturation, making it more prone to interact with oxygen atoms, while the top-Mn_{5c} site is slightly more saturated but could serve as a potential active site. The bridge-Mn_{4c} site, located between two Mn_{4c} atoms, offers unique interaction possibilities due to its ability to engage two Mn centers simultaneously.

3.2. Adsorption of Oxidant Molecules on β-MnO_2. It has previously been reported that surface OH species, generated by the added oxidants, play an important role in the HMF oxidation reaction.[8,60−62] It is crucial to understand the effect of oxidant molecules on the production of surface OH species under reaction conditions. To obtain such insight, we first study the adsorption of oxidant molecules on the catalyst's surface including O_2, H_2O_2, and TBHP. Then, we calculated the energy barrier and reaction energy for the decomposition of oxidant molecules on the β-MnO_2 surface (Section 3.3). Lastly, we constructed an ab initio thermodynamic model to predict OH coverages generated by different oxidants under experimental conditions (Section 3.4).

First, we explored the adsorption of oxidant molecules, where various adsorbed configurations are considered, as detailed in the Supporting Information (SI) Section S1. The stability of the adsorbed molecules can be determined by calculating the adsorption energies, E_{ads}, as follows

$$E_{ads} = E_{gas-MnO_2} - E_{MnO_2} - E_{gas} \quad (1)$$

where $E_{gas\text{-}MnO_2}$ is the total energy of the surface with an adsorbed oxidant molecule, E_{MnO_2} is the total energy of the bare β-MnO_2(110) surface, and E_{gas} is the total energy of an isolated oxidant molecule. The more negative E_{ads} indicates a stronger interaction between the molecule and the surface.

As shown in Figure 2 and summarized in Table S1, we find that all considered oxidant molecules prefer to adsorb with

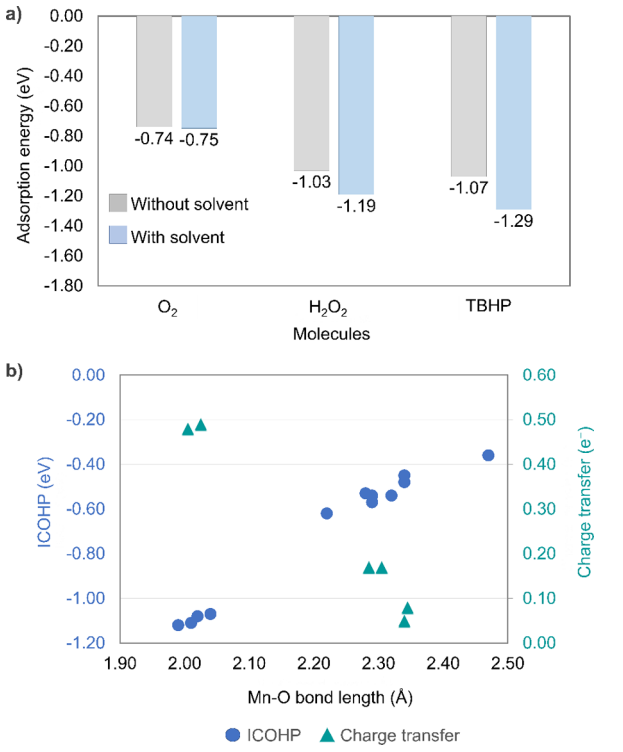

Figure 2. (a) Adsorption energies of oxidant molecules with and without treatment of the implicit solvent model. (b) Correlation between Mn−O bond length (Å), integrated crystal orbital Hamilton population (ICOHP) (eV), and charge transfer (e^-).

both of the O atoms of the oxidant molecule located on the bridge-Mn_{4c} site due to the unsaturated nature of two Mn_{4C} atoms, as shown in Figure S1. The calculated adsorption energies reveal that TBHP (E_{ads} = −1.29 eV) interacts most strongly with the surface, which is comparable to that of H_2O_2 (E_{ads} = −1.19 eV), while O_2 (E_{ads} = −0.75 eV) adsorbs somewhat weaker than the other two molecules. In addition, adsorption of oxidant molecules becomes stronger in the presence of solvent media treated using the implicit solvent model, as shown in Figure 2a.

Next, we further analyzed the correlation between the adsorption strength and the structural and electronic properties of the adsorbed molecules. As shown in Figure S2, the projected density of states of the adsorbed systems reveals good overlap between the O 2p states of the oxidants and Mn 3d states of the surface at the valence band for all oxidant molecules.

To quantify the overlapping bonding interactions at the valence band, we calculated the integrated values of the Crystal Orbital Hamilton Population (ICOHP).[37,63,64] More negative ICOHP values indicate stronger bonding interactions. Our analysis reveals a strong correlation between the ICOHP values and the bond length between the surface Mn atom and the oxygen atom of the adsorbed molecule (Mn−O bond); i.e., a more negative ICOHP value corresponds to a shorter Mn−O bond length, indicating stronger bonding, as shown in Figure 2b and Table S2.

https://doi.org/10.1021/acsomega.4c10253
ACS Omega 2025, 10, 12097−12108

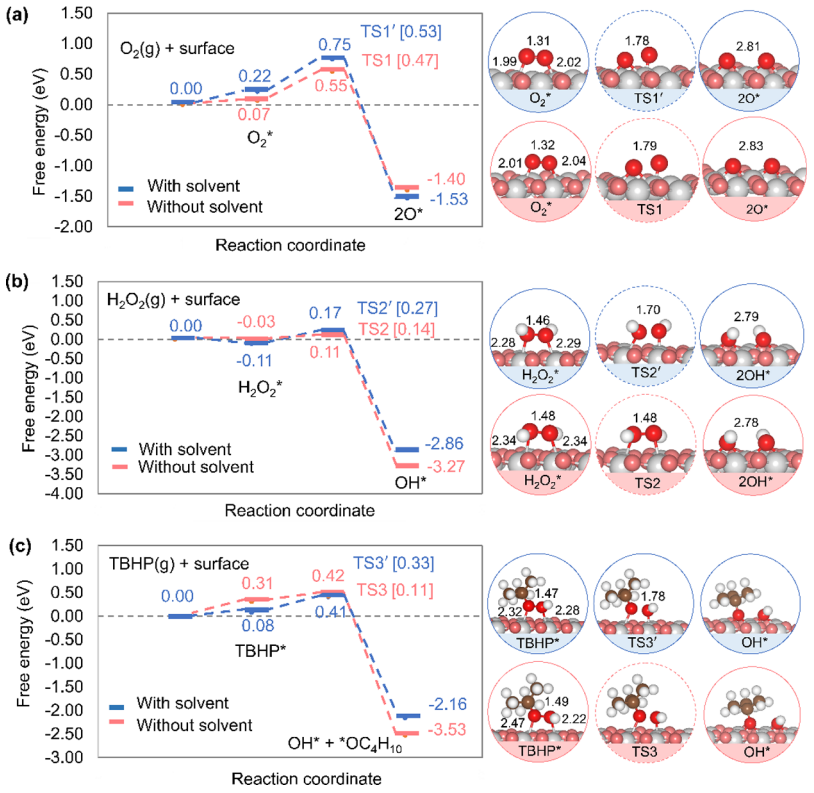

Figure 3. Free energy profiles and the most stable configurations of transition states (TS), and intermediates for (a) O_2, (b) H_2O_2, and (c) TBHP decomposition on the β-MnO_2(110) surface at 393 K with and without treatment of an implicit solvent model. The $\Delta G_i^{\ddagger}$ values in eV are displayed in square brackets.

Furthermore, the structure of the adsorbed molecules is closely related to the degree of charge transfer. As shown in Figure 2b, shorter Mn−O bond lengths are associated with a higher degree of charge transfer. These findings suggest that the electronic properties, including the ICOHP values and the extent of charge transfer during adsorption, are strongly influenced by the structural characteristics of the adsorbed oxidant molecules. It is worth noting that the charge transfer analysis shows that after O_2 is adsorbed, electrons transfer from the catalyst to the O_2 molecule. In contrast, for H_2O_2 and TBHP, the electrons transfer from these molecules to the catalyst's surface, as shown in Figure S1. This result indicates that molecular oxygen (O_2) is an electron acceptor due to its high electronegativity. When O_2 adsorbs onto the β-MnO_2(110) surface, it interacts with Mn atoms that have partially filled d-orbitals, which leads to the transfer of electrons from the catalyst surface to the oxygen molecule. Additionally, the surface of the β-MnO_2(110) catalyst has Mn atoms that are not fully coordinated, which means that they have dangling bonds or active sites that can interact with adsorbed species. These sites are capable of accepting or donating electrons, resulting in electron transfer that helps stabilize the adsorbed O_2, H_2O_2, and TBHP molecules. It is noteworthy that the active site on the β-MnO_2(110) surface is suggested to involve Mn and O atoms as Lewis acid−base pairs.[24] They are responsible for the activation of C−H bonds in various molecules.[65−67] In addition, charge transfer supports the idea that Mn active sites act as Lewis acid sites, as after the adsorption of TBHP and H_2O_2, charge transfer occurs from the oxidant molecules to the Mn center. This calculation shows electron-deficient regions at the active sites.

Interestingly, we found no clear correlation between the adsorption energies of the adsorbed molecules and their electronic or structural properties. For example, although O_2 has the weakest adsorption energy among the oxidants considered, it shows the shortest Mn−O bond length, the most negative ICOHP value, and the highest degree of charge transfer. In contrast, TBHP and H_2O_2 display relatively longer Mn−O bond lengths, less negative ICOHP values, and lower degrees of charge transfer, yet they have stronger adsorption energies. These results suggest that the stronger adsorption of TBHP and H_2O_2 is primarily due to nonbonding interactions, which involve a lower degree of charge redistribution. The calculated adsorption energy without van der Waals corrections supports this statement, where the adsorption energy of O_2 (−1.19 eV) becomes the most stable, followed by H_2O_2 (−1.15 eV) and TBHP (−0.88 eV).

It is expected that the adsorption of oxidant molecules would result in the activation of the O−O bond. For example, when O_2 adsorbs onto the surface, its O−O bond lengthens from 1.233 to 1.309 Å. This elongation can facilitate the cleavage of the O−O bond, leading to the formation of surface OH species. This observation agrees with previous studies that when O_2 adsorbs onto the β-MnO_2 surface, it takes on a superoxo-like O_2^- state, characterized by vibrational frequencies near 1140 cm^{-1} and an O−O bond length of 1.33 Å.[39] Nevertheless, the adsorption energy of O_2 on β-MnO_2(110) is relatively weaker than that adsorbed on other metal oxides including Co_3O_4(001) (−1.91 eV),[68] Au/RuO_2(110) (−1.78 eV),[69] α-MnO_2(211) (−2.88 eV),[70] and Zr/α-MnO_2(211) (−3.13 eV).[70]

In contrast, the adsorption of H_2O_2 and TBHP results in a slight shortening of their O−O bonds—from 1.483 to 1.479 Å

https://doi.org/10.1021/acsomega.4c10253
ACS Omega 2025, 10, 12097−12108

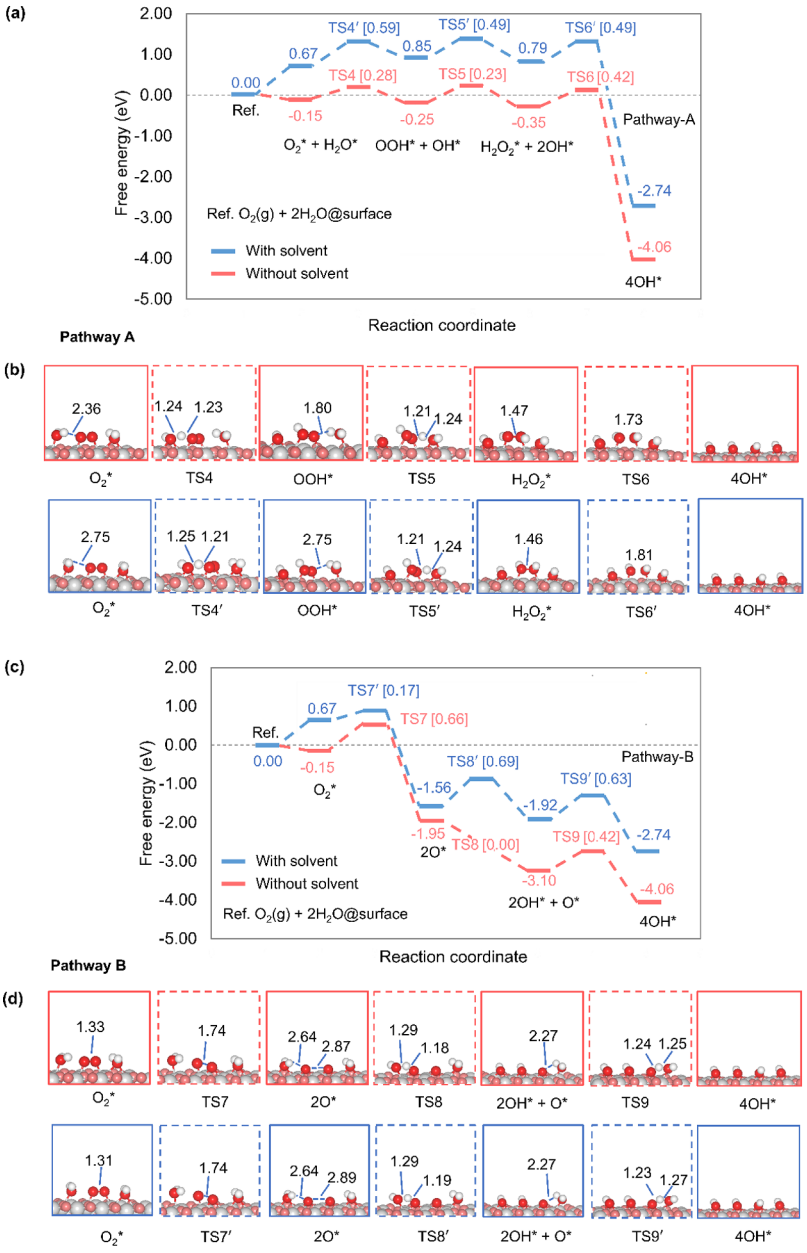

Figure 4. Free energy profiles at 393 K for the OH formation on β-MnO_2 from the dissociation of coadsorption between O_2* and H_2O* molecules with structures of transition states and intermediates for (a,b) pathway-A and (c,d) pathway-B. The $\Delta G_i^{\ddagger}$ barriers in eV are displayed in square brackets. Bond lengths are given in Å.

for H_2O_2 and from 1.493 to 1.490 Å for TBHP (Figure S1 and Table S1). Despite this slight bond shortening, the cleavage of the O−O bond in H_2O_2 and TBHP is still expected to be more favorable than that of O_2, owing to their inherently longer initial O−O bond lengths.

Based on the calculated results, we find that the relatively strong adsorption of H_2O_2 and TBHP is attributed to nonbonding interactions, while the effect of nonbonding interactions for smaller molecules like O_2 is less pronounced. Furthermore, O_2 adsorption leads to significant O−O bond lengthening, facilitating cleavage, whereas H_2O_2 and TBHP exhibit slight bond shortening but still favor O−O bond cleavage due to their longer initial bond length. The mechanism and energetics of the O−O bond activation are discussed in Section 3.3.

3.3. Activation of Oxidant Molecules upon Adsorption. The activation of the O−O bond in oxidant molecules is a crucial step for the formation of surface OH species. In this section, we explore the mechanisms and energy barriers involved in the cleavage of adsorbed oxidant molecules to produce surface OH species. We consider two different pathways: (i) direct O−O bond dissociation, and (ii) for the adsorbed O_2 molecule, an additional pathway involving the reaction of O_2 with H_2O to form surface OH species.

3.3.1. Direct O−O Bond Dissociation of Oxidant Molecule. The cleavage of the O−O bond of adsorbed O_2, H_2O_2, and TBHP takes place over the bridge-Mn_{4c} sites. Their free energy profiles, structures of key intermediates, transition states, and an energy profile at 0 K are shown in Figures 3 and S3. Activation energies (E_a and $\Delta G_i^{\ddagger}$) and reaction energies (ΔE and ΔG_r) for all elementary steps of the decomposition of

https://doi.org/10.1021/acsomega.4c10253
ACS Omega 2025, 10, 12097−12108

O_2, H_2O_2, and TBHP molecules on the β-MnO_2(110) surface are listed in Table S3.

First, the direct O−O bond cleavage of O_2 ($O_2^* \rightarrow 2O^*$) is thermodynamically favorable, with an exergonic reaction free energy of −1.47 eV and a barrier of 0.47 eV, as shown in Figure 3a. The inclusion of the implicit solvation model stabilizes the adsorbed O* intermediate, resulting in a more exergonic reaction of −1.75 eV, while it destabilizes the O_2* and TS of O−O bond breaking, leading to an increase in the energy barrier to 0.53 eV. Our calculated O_2 dissociation barrier is lower than that on Co_3O_4(001) (1.69 eV),[68] Co_3O_4(110) (4.02 eV),[68] and Co_3O_4(111) (3.58 eV).[68] This result suggests that the formation of 2O* on the β-MnO_2(110) surface is more kinetically favorable than that on other metal oxides.

As expected, the O−O bond for H_2O_2 and TBHP is both thermodynamically and kinetically more favorable than that of O_2. For H_2O_2, the reaction has a free energy of −3.27 eV with a low barrier of 0.14 eV, while for TBHP, the reaction free energy is −3.53 eV with an even lower barrier of 0.11 eV. This is due to their inherently longer O−O bonds of adsorbed H_2O_2 (1.48 Å) and TBHP (1.49 Å) compared with that of adsorbed O_2 (1.32 Å), which result in lower bond dissociation barriers and more exergonic reaction energies, as shown in Figure 3.

The inclusion of solvent effects generally raises the barriers for the scission of the O−O bond while destabilizing the intermediates formed during bond cleavage for both H_2O_2 and TBHP, as shown in Figure 3b,c. This results in increased energy barriers for both H_2O_2 and TBHP, which rise to 0.27 and 0.33 eV, respectively. The destabilization of the bond-breaking intermediates in the solvent environment also makes the reactions less exergonic, with reaction energies decreasing to −2.86 eV for H_2O_2 and −2.16 eV for TBHP. This suggests that the dielectric constant applied using implicit solvent model not only makes the bond cleavage process less favorable by increasing the energy barriers but also reduces the overall driving force of the reaction by decreasing the stability of the intermediate states. Consequently, the solvent environment alters both the kinetics and thermodynamics of the bond cleavage process, making it less favorable than that in the gas phase. It is noteworthy that the O−O bond cleavage of H_2O_2 on the β-MnO_2 surface has an energy barrier lower than that on $YFeO_3$ (1.41 eV),[71] Ti-$YFeO_3$ (0.98 eV),[71] and Fe_3O_4(311) (0.76 eV).[72]

Overall, the O−O bond cleavage of O_2, H_2O_2, and TBHP on the β-MnO_2(110) surface plays an important role in generating active surface O and OH species essential for oxidation processes. H_2O_2 and TBHP exhibit more favorable cleavage with lower energy barriers and more exergonic reactions than O_2 due to their longer O−O bonds. The presence of a solvent generally increases the energy barriers and decreases the exergonicity of the reactions by destabilizing intermediates, making the cleavage less favorable than that in the gas phase. Despite this, β-MnO_2(110) shows more favorable O_2 and H_2O_2 dissociation kinetics compared to other metal oxides, suggesting its potential for catalytic applications. Alternatively, the surface OH groups from adsorbed O_2 molecules can be produced by reacting with H_2O molecules in the solvent. The detailed mechanisms of these reactions are discussed in the next section.

3.3.2. Formation of Surface OH Species via O_2 and H_2O Reaction. The surface OH species can be generated not only through the direct cleavage of the O−O bonds of oxidant molecules but also via the reaction of adsorbed O_2 with H_2O. Two proposed mechanisms were explored in this study including pathway-A via formation of the H_2O_2 intermediate as

i. $O_2^* + H_2O^* \rightarrow OOH^* + OH^*$
ii. $OOH^* + OH^* + H_2O^* \rightarrow H_2O_2^* + 2OH^*$
iii. $H_2O_2^* + 2OH^* \rightarrow 4OH^*$

and pathway-B via the direct O−O bond cleavage of the adsorbed O_2 molecule:

i. $O_2^* \rightarrow 2O^*$
ii. $2O^* + H_2O^* \rightarrow 2OH^* + O^*$
iii. $2OH^* + O^* + H_2O^* \rightarrow 4OH^*$

The relative energy profile at 0 K, along with the most stable configurations, including transition states (TS) and intermediates, for pathways A and B, is shown in Figure S4, where all barriers and reaction energies are summarized in Table S3.

The free energy profile of pathway-A (Figure 4a) shows that the initial step involves the transfer of H from H_2O* to O_2* to form OOH* and OH* intermediates (step-i). This step is exergonic with a free energy change of −0.10 eV and a barrier of 0.28 eV. Then, the OOH* intermediate further reacts with an additional H_2O molecule to produce H_2O_2* and another OH* (step-ii), which is slightly exergonic with a free energy change of −0.09 eV and a relatively low barrier of 0.23 eV. Finally (step-iii), the H_2O_2* intermediate undergoes O−O bond breaking to form two more OH groups on the surface, with a barrier of 0.42 eV and an exergonicity of −3.72 eV.

It is noteworthy that the OOH* formation via step-i on the β-MnO_2 surface exhibits a lower energy barrier compared to the O−H bond breaking of H_2O_2 to form OOH* on the Fe_3O_4(311) (E_a = 0.52 eV),[72] $YFeO_3$ (E_a = 1.08 eV),[71] and Ti-$YFeO_3$ (E_a = 0.40 eV)[71] surfaces. This result implies that the coadsorption between O_2* and H_2O* can easily produce OOH* species on the β-MnO_2 surface.

As discussed in the previous section, the inclusion of an implicit solvent model generally destabilizes intermediates and transition states. Similarly, the inclusion of an implicit solvent raises both the reaction energies and barriers for all elementary steps. For example, for step-i, the inclusion of the implicit solvent model destabilizes the H_2O−O_2 configuration, causing two H atoms to point away from the $*O_2$, as shown in Figure 4b. This leads to an increase in the distance between H atoms of H_2O and $*O_2$ from 2.36 to 2.75 Å, resulting in a higher barrier for hydrogen transfer in step-i and step-ii. In addition, for the O−O bond breaking of H_2O_2* in the step-iii, the implicit solvent model destabilizes both the H_2O_2* and TS6′ structures, leading to the formation of the less stable 4OH*. It should be noted that the O−O bond dissociation of H_2O_2 via TS6' with the coadsorption of OH* on the surface has a barrier lower than that of direct O−O bond breaking via TS2'. This result indicates that in addition to the implicit solvation model, the hydroxyl groups surrounding H_2O_2* play a crucial role in promoting O−O bond dissociation. Consequently, the barriers for steps i, ii, and iii increase to 0.59, 0.49, and 0.49 eV, respectively. The overall reaction also become less exergonic, with a free energy change of −2.74 eV.

We then considered the OH production via pathway-B in the gas phase, where it starts with the O−O bond cleavage of adsorbed O_2 in the first step (step-i), as shown in Figure 4c. As previously discussed, direct O−O bond breaking is rather difficult, with a high barrier of 0.66 eV, but the formation of

https://doi.org/10.1021/acsomega.4c10253
ACS Omega 2025, 10, 12097−12108

O* is highly stable, with a reaction free energy of −1.80 eV. Next (steps ii and iii), H atoms from two H_2O* transfer to adjacent O* species, producing four OH* on the surface. The first H transfer (step-ii) proceeds without a barrier, while the second one (step-iii) exhibits a barrier of 0.42 eV, with reaction free energies of −1.27 and −0.84 eV, respectively.

It is noteworthy that the implicit solvation model destabilizes the initial structures of both H_2O* and O_2*, resulting in a decrease in the O−O bond distance from 1.33 to 1.31 Å, as illustrated in Figure 4d. The barrier for direct O−O bond cleavage is dramatically reduced to 0.17 eV when using an implicit solvent model. This reduction can be attributed to the substantial destabilization of the coadsorbed O_2* and H_2O* intermediates, while the destabilization of the TS is less pronounced. In addition, the subsequent two steps of hydrogen transfer (steps ii and iii) from H_2O* to O* exhibit higher energy barriers of 0.69 and 0.63 eV, with less exergonic reaction energies of −0.35 and −0.82 eV, respectively. The cleavage of the O−O bond to form OH via pathway B shows a high energy barrier due to the destabilization of H_2O surrounding the O* species. In addition, the implicit solvent model consistently leads to higher barriers and reduced exergonicity throughout all calculations in pathway B. Our results reveal that the coadsorbed O_2* and H_2O* facilitate an energetically favorable pathway that efficiently promotes the dissociation of H_2O and stabilizes the resulting O* and OH*, which corresponds with previous DFT calculations.[26] In addition, O anions and metal cations on metal oxide surfaces could act as Lewis pairs, facilitating H_2O dissociation and promoting OH* formation on the surface.[25,27]

3.4. Thermodynamics Model of OH Coverages on β-MnO_2. In this section, we determined the surface OH coverages generated from different oxidant species using the ab initio thermodynamics model.[73−76] First, we calculated OH formation energies ($E_{f,OH}$) at various OH coverages for all considered oxidant species according to the following chemical reactions.

For O_2

$$O_2 + 2H_2O + * \rightarrow (OH)_4^*$$

$$E_{f,OH}^{O_2} = E_{(OH)_4^*} - (E_{O_2} + 2E_{H_2O} + E_*) \quad (2)$$

For H_2O_2

$$H_2O_2 + * \rightarrow (OH)_2^*$$

$$E_{f,OH}^{H_2O_2} = E_{(OH)_2^*} - (E_{H_2O_2} + E_*) \quad (3)$$

For TBHP

$$(CH_3)_3COOH + 2* \rightarrow (CH_3)_3CO^* + OH^*$$

$$E_{f,OH}^{TBHP} = (E_{(CH_3)_3CO^*} + E_{OH^*}) - (E_{(CH_3)_3COOH} + 2E_*) \quad (4)$$

where E_{OH^*}, $E_{(OH)_2^*}$, and, $E_{(OH)_4^*}$ are the total energies of the surface with one, two, and four OH species, respectively. E_* and $E_{(CH_3)_3CO^*}$ are the total energies of the β-MnO_2 surface in the absence and presence of the $(CH_3)_3CO$* intermediate. E_{O_2}, E_{H_2O}, $E_{H_2O_2}$, and $E_{(CH_3)_3COOH}$ are the total energies of isolated O_2, H_2O, H_2O_2,and TBHP molecules, respectively.

To examine the effect of surface coverage (θ), we calculated the OH formation energy as a function of OH coverage up to a monolayer, as shown in Figures S5−S8. The surface coverage of OH (θ) can be calculated using the following equation.

$$\theta = \frac{N_{OH}}{N_{Mn-active\ site}} \quad (5)$$

where N_{OH} and $N_{Mn\text{-}active\ site}$ represent the numbers of adsorbed OH species and Mn active sites on the β-MnO_2 surface, respectively. To obtain a monolayer coverage, we first adsorb OH at its most stable adsorption site at bridge-Mn_{4c}. After the bridge-Mn_{4c} site is fully occupied, OH is adsorbed at the top-Mn_{5c} site until the monolayer coverage is obtained.

As shown in Figure 5, we find that as the OH coverage increases, the OH formation energy also rises. Although the reaction energy per OH molecule remains negative, the initial OH coverage is more energetically favorable than higher coverages. Figure 5 reveals that the OH formation energy from O_2 dissociation (−5.85 eV) is more stable than that from TBHP (−3.79 eV) and H_2O_2 (−3.73 eV) at a low OH coverage of θ = 0.25. At a high OH coverage up to a monolayer, the OH formation energy from TBHP dissociation (−3.14 eV) is more stable than those from O_2 (−2.96 eV) and H_2O_2 (−2.42 eV). This implies that at a high OH coverage up to a monolayer, the OH formation energy from TBHP dissociation is more stable than that from O_2 and H_2O_2. This could be due to the stronger interaction between the $(CH_3)_3CO$ intermediate and the β-MnO_2 surface upon the dissociation of TBHP. Such stably adsorbed $(CH_3)_3CO$ intermediate could lead to further stabilization of the produced OH* at high coverages.

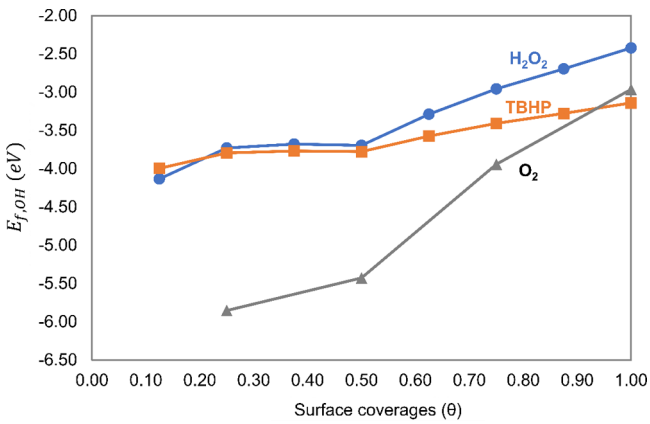

Figure 5. Calculated reaction energy per oxidant molecules for the dissociation of oxidant molecules on the β-MnO_2 surface as a function of the surface coverage of OH with solvent effect.

Next, to account for the effect of temperature and pressure on the production of surface OH species, we employed the ab initio thermodynamic model to determine the OH coverages on the surface. We computed and compared the surface free energy as a function of temperature and pressure, $\sigma(T, P)$, at various OH coverages as follows:

For O_2

$$\sigma(T, P) = \frac{1}{A}[E_{f,OH}^{O_2} - \Delta\mu_{O_2}(T, P) - 2\Delta\mu_{H_2O}(T, P)] \quad (6)$$

For H_2O_2

https://doi.org/10.1021/acsomega.4c10253
ACS Omega 2025, 10, 12097−12108

$$\sigma(T, P) = \frac{1}{A}[E_{f,OH}^{H_2O_2} - \Delta\mu_{H_2O_2}(T, P)] \quad (7)$$

For TBHP

$$\sigma(T, P) = \frac{1}{A}[E_{f,OH}^{TBHP} - \Delta\mu_{(CH_3)_3COOH}(T, P)] \quad (8)$$

where A is the surface area. The chemical potential of oxidant molecules, which includes the temperature- and pressure-dependent free energy contributions of isolated oxidant molecules, is described by $\Delta\mu_{gas}(T, P$; gas = O_2, H_2O, H_2O_2, $(CH_3)_3COOH)$ and was calculated from first-principles using rotational, translational, and vibrational partition functions of isolated oxidant molecules. In addition, the pressure dependence of $\Delta\mu_{gas}(T, P)$ is obtained assuming the gas phase is ideal and can be calculated as

$$\Delta\mu_{gas}(T, P) = \Delta\mu_{gas}(T, P_0) + k_B T \ln\frac{P}{P_0} \quad (9)$$

where P_0 = 1 atm, and k_B and P are the Boltzmann constant and the pressure of the gas molecule, respectively. We plotted the pressure of oxidant molecules against the chemical potential at various temperatures to reveal a relationship between experimental conditions and DFT calculations, as shown in Figure 6. The region indicated by the green dashed lines represents the chemical potential of oxidant molecules under the experimental conditions[1,8] of HMF oxidation reactions, where the reaction is operated at 10 bar with temperatures ranging from 350 to 400 K.

Then, we determined the OH coverages on the β-MnO_2 surface from the estimated chemical potential of oxidants under the reaction conditions of HMF oxidation. As shown in Figure 7a, computations reveal that as the chemical potential of O_2 increases, the surface energy of OH coverages becomes more negative. This indicates that the greater chemical potential of O_2, i.e., the higher concentration and more reactive O_2 oxidant, the more stable OH production on the surface. Under the reaction conditions, the predicted OH coverage is 0.75.

The OH coverage resulting from H_2O_2 and TBHP dissociation is represented in Figure 7b,c, respectively. We find that the OH coverage on the β-MnO_2 surface from H_2O_2 and TBHP (θ = 1.00) dissociation is higher than that from O_2 (θ = 0.75) under the reaction conditions. The H_2O_2 and TBHP molecules can generate an OH monolayer on the β-MnO_2 surface under the reaction conditions. However, TBHP can generate a higher OH coverage on the catalyst surface with a lower surface energy than H_2O_2 and O_2. This result implies that the high OH coverage from TBHP on the β-MnO_2 surface is thermodynamically more favorable than that from H_2O_2 and O_2 under the reaction condition.

To better illustrate the relationship between OH coverage and reaction conditions, we constructed a phase diagram using the ab initio thermodynamic model, as described above. As shown in Figure 8a, for OH formation resulting from O_2 dissociation, the β-MnO_2(110) surface was occupied by OH at a 0.75 coverage under the reaction conditions at 10 bar and temperatures ranging from 350 to 400 K. At higher temperatures, the OH coverage changed from 0.75 to 0.50 at temperatures higher than 400 K, as shown in Figure 8a. For the H_2O_2 oxidant, the β-MnO_2(110) surface exhibits full OH coverage under the reaction conditions. However, as the temperature increases, particularly in the region above 400 K,

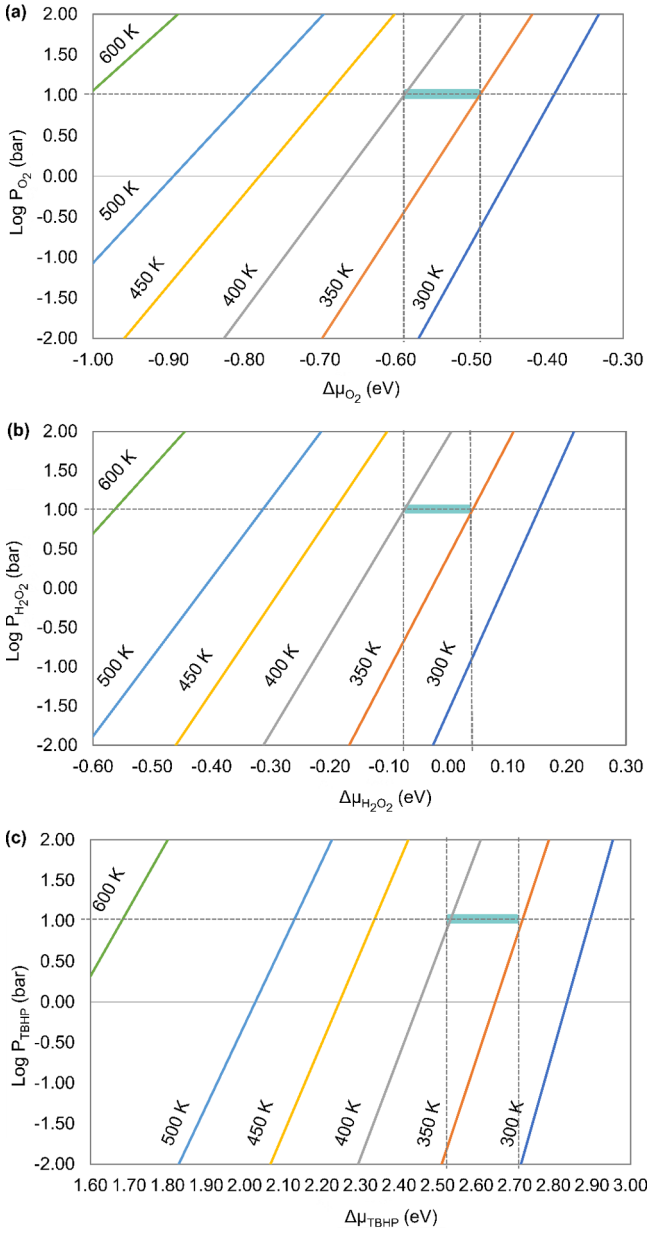

Figure 6. Pressure of oxidant molecules against the different chemical potentials at different temperatures of (a) O_2, (b) H_2O_2, and (c) TBHP.

the coverage decreases from 1.00 to 0.88 before halving at temperatures exceeding 800 K, as depicted in Figure 8b. For the TBHP oxidant, Figure 8c reveals that the OH coverage changes from 1.00 to 0.94 at temperatures higher than 900 K. This result implies that using the TBHP oxidant leads to the formation of OH on the surface constituting a monolayer and exhibits a higher OH coverage compared to H_2O_2 and O_2 at high temperatures. Although TBHP shows higher dissociation barriers (0.33 eV) than H_2O_2 (0.27 eV), resulting in slower OH production kinetics, such OH production is thermodynamically more favorable when TBHP is used as the oxidant. The slower OH production kinetics of TBHP decomposition are highly suitable for the oxidation reaction, as they enable a continuous supply of OH throughout the process. This steady OH availability contributes to the high selectivity of FDCA (96.3%) during the oxidation of HMF with the Cu-doped

https://doi.org/10.1021/acsomega.4c10253
ACS Omega 2025, 10, 12097−12108

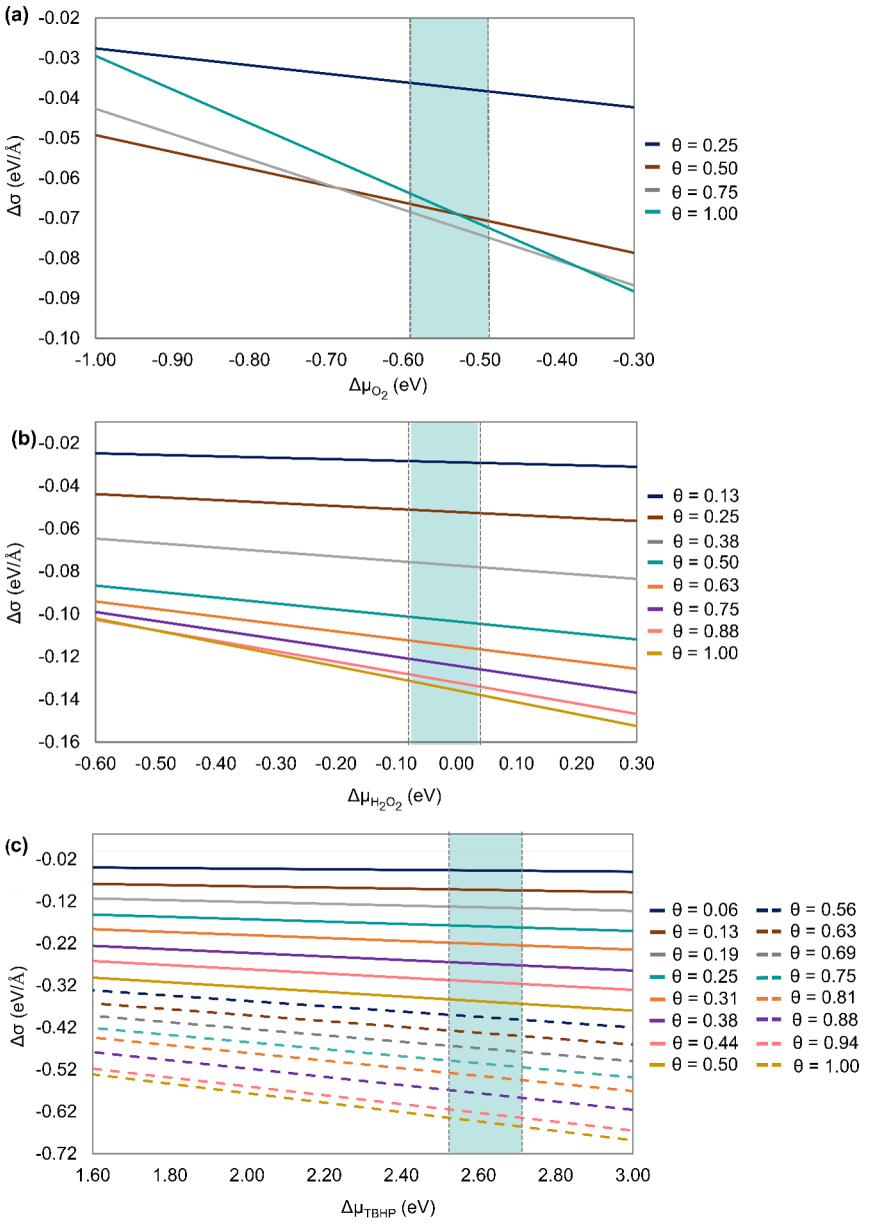

Figure 7. Surface energy of OH formation versus chemical potential of oxidants at various OH coverages on the β-MnO_2 surface within the treatment of the implicit solvent model resulting from the dissociation of (a) coadsorption between O_2 and H_2O, (b) H_2O_2, and (c) TBHP.

MnO_2 catalyst.[8] It is noteworthy that although TBHP is identified as a more efficient oxidizing agent for generating OH coverage on the β-MnO_2 surface compared to O_2 and H_2O_2, the use of TBHP has been greatly limited due to safety concerns over its shipping, handling, and storage, particularly at the production scale.[77]

4. CONCLUSIONS

In this work, we employed density functional theory calculations and ab initio thermodynamic modeling to study the effects of different oxidant molecules, including O_2, H_2O_2, and TBHP, on the kinetics and thermodynamics of OH production on the β-$MnO_2(110)$ surface. Computations reveal that TBHP is the most effective oxidant for stable OH coverage, with low bond dissociation barriers and highly exergonic reactions, followed closely by H_2O_2, while O_2 is the kinetically least favorable.

To further illustrate the OH coverage under different reaction conditions, we constructed phase diagrams that show the effects of the temperature and pressure on OH formation for each oxidant. Under the reaction conditions of HMF oxidation, using O_2 as an oxidant yields an OH coverage of 0.75 at 10 bar and 350−400 K. This coverage decreases to 0.50 as temperatures exceed 400 K, indicating that O_2 is effective within moderate temperature ranges. In contrast, H_2O_2 maintains full OH coverage (1.00) under the reaction conditions, although the coverage reduces to 0.88 as temperatures exceed 400 K and further reduces at 800 K, suggesting temperature sensitivity. TBHP, the most robust oxidant, maintains a near-monolayer OH coverage of 1.00 under reaction conditions and decreases only slightly (to 0.94) at temperatures above 900 K, indicating its high stability across a broad temperature range. Overall, these findings reveal TBHP as the most favorable oxidant for generating a stable and high OH coverage on β-$MnO_2(110)$, making it an effective

https://doi.org/10.1021/acsomega.4c10253
ACS Omega 2025, 10, 12097−12108

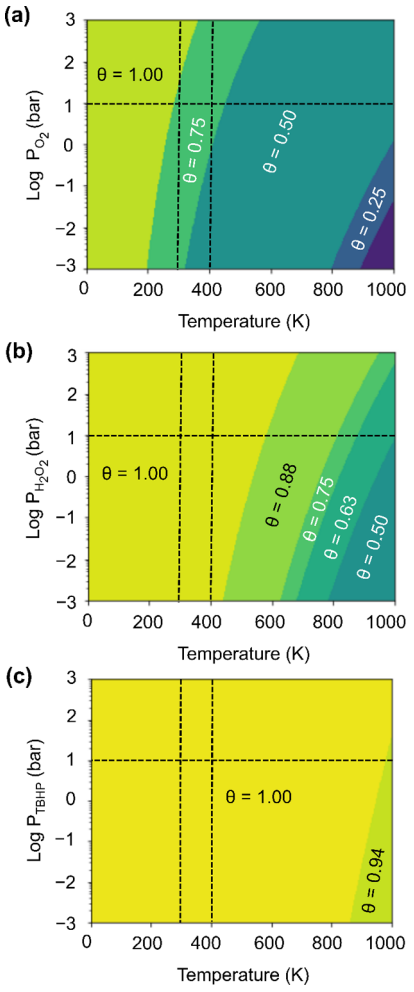

Figure 8. Phase diagrams of OH coverages as a function of pressure of oxidant molecules and temperature resulting from the dissociation of (a) coadsorption between O_2 and H_2O_2, (b) H_2O_2, and (c) TBHP. The region between the dashed lines represents the experimental conditions for HMF oxidation reactions at 10 bar and temperatures ranging from 350 to 400 K.

oxidant for oxidative catalytic applications such as the HMF oxidation process.

■ ASSOCIATED CONTENT

Supporting Information

The Supporting Information is available free of charge at https://pubs.acs.org/doi/10.1021/acsomega.4c10253.

Adsorption of oxidant molecules and activation of oxidant molecules on β-MnO_2 and effect of OH coverage on β-MnO_2 (PDF)

■ AUTHOR INFORMATION

Corresponding Authors

Anchalee Junkaew − *National Nanotechnology Center (NANOTEC), National Science and Technology Development Agency (NSTDA), Pathum Thani 12120, Thailand;* orcid.org/0000-0002-3193-1110; Email: anchalee@nanotec.or.th

Suwit Suthirakun − *School of Chemistry, Institute of Science, Suranaree University of Technology, Nakhon Ratchasima 30000, Thailand;* orcid.org/0000-0002-6590-6343; Email: suthirak@sut.ac.th

Authors

Bunrat Tharat − *School of Chemistry, Institute of Science, Suranaree University of Technology, Nakhon Ratchasima 30000, Thailand*

Panupol Untarabut − *School of Physics, Institute of Science, Suranaree University of Technology, Nakhon Ratchasima 30000, Thailand;* Present Address: Institut de Recherche sur les Céramiques (IRCER), UMR CNRS 7315-Université de Limoges, Limoges 87068, France

Complete contact information is available at: https://pubs.acs.org/10.1021/acsomega.4c10253

Notes

The authors declare no competing financial interest.

■ ACKNOWLEDGMENTS

This project is funded by Suranaree University of Technology (SUT) and the NSRF via the Program Management Unit for Human Resources and Institutional Development, Research and Innovation (PMU-B) (grant number B13F660067). We further acknowledge the funding from (i) Suranaree University of Technology (SUT), (ii) Thailand Science Research and Innovation (TSRI), and (iii) National Science, Research, and Innovation Fund (NSRF) (NRIIS Project Number 204271). A.J. would like to acknowledge the National Science, Research and Innovation Fund, Thailand Science Research and Innovation (TSRI) (Grant No.: FFB680075/0337). We acknowledge NSTDA Supercomputer Center (ThaiSC) and Nanoscale Simulation Laboratory at National Nanotechnology Center (NANOTEC) for computing resources.

■ REFERENCES

(1) Tharat, B.; Ngamwongwan, L.; Seehamongkol, T.; Rungtaweevoranit, B.; Nonkumwong, J.; Suthirakun, S.; Faungnawakij, K.; Chanlek, N.; Plucksacholatarn, A.; Nimsaila, W.; Prommin, C.; Junkaew, A. Hydroxy and surface oxygen effects on 5-hydroxymethylfurfural oxidation to 2,5-furandicarboxylic acid on β-MnO_2: DFT, microkinetic and experiment studies. *Nanoscale* **2024**, *16*, 678.

(2) Liu, Y.; Ma, H.-Y.; Lei, D.; Lou, L.-L.; Liu, S.; Zhou, W.; Wang, G.-C.; Yu, K. Active oxygen species promoted catalytic oxidation of 5-hydroxymethyl-2-furfural on facet-specific Pt nanocrystals. *ACS Catal.* **2019**, *9*, 8306−8315.

(3) Davis, S. E.; Zope, B. N.; Davis, R. J. On the mechanism of selective oxidation of 5-hydroxymethylfurfural to 2,5-furandicarboxylic acid over supported Pt and Au catalysts. *Green Chem.* **2012**, *14*, 143−147.

(4) Tamura, H.; Mita, K.; Tanaka, A.; Ito, M. Mechanism of hydroxylation of metal oxide surfaces. *J. Colloid Interface Sci.* **2001**, *243*, 202−207.

(5) Chen, C.-T.; Nguyen, C. V.; Wang, Z.-Y.; Bando, Y.; Yamauchi, Y.; Bazziz, M. T. S.; Fatehmulla, A.; Farooq, W. A.; Yoshikawa, T.; Masuda, T.; Wu, K. C. W. Hydrogen peroxide assisted selective oxidation of 5-hydroxymethylfurfural in water under mild conditions. *ChemCatChem.* **2018**, *10*, 337−337.

(6) Teong, S. P.; Li, X.; Zhang, Y. Hydrogen peroxide as an oxidant in biomass-to-chemical processes of industrial interest. *Green Chem.* **2019**, *21*, 5753−5780.

(7) Mittal, N.; Kaur, M.; Singh, V. Mild and selective catalytic oxidation of 5-HMF to 2,5-FDCA over metal loaded biomass derived graphene oxide using hydrogen peroxide in aqueous media. *Mol. Catal.* **2023**, *546*, No. 113223.

(8) Cheng, F.; Guo, D.; Lai, J.; Long, M.; Zhao, W.; Liu, X.; Yin, D. Efficient base-free oxidation of 5-hydroxymethylfurfural to 2,5-furandicarboxylic acid over copper-doped manganese oxide nanorods with tert-butanol as solvent. *Front. Chem. Sci. Eng.* **2021**, *15*, 960−968.
(9) Hayashi, E.; Komanoya, T.; Kamata, K.; Hara, M. Heterogeneously-catalyzed aerobic oxidation of 5-hydroxymethylfurfural to 2,5-furandicarboxylic acid with MnO_2. *ChemSusChem* **2017**, *10*, 654−658.
(10) Hayashi, E.; Oba, F.; Yamaguchi, Y.; Kamata, K.; Tsunoda, N.; Kumagai, Y.; Hara, M. Effect of MnO_2 crystal structure on aerobic oxidation of 5-hydroxymethylfurfural to 2,5-furandicarboxylic Acid. *J. Am. Chem. Soc.* **2019**, *141*, 890−900.
(11) Li, S.; Su, K.; Li, Z.; Cheng, B. Selective oxidation of 5-hydroxymethylfurfural with H_2O_2 catalyzed by a molybdenum complex. *Green Chem.* **2016**, *18*, 2122−2128.
(12) Rao, K. T. V.; Rogers, J. L.; Souzanchi, S.; Dessbesell, L.; Ray, M. B.; Xu, C. C. Inexpensive but highly efficient Co-Mn mixed-oxide catalysts for selective oxidation of 5-hydroxymethylfurfural to 2,5-furandicarboxylic acid. *ChemSusChem* **2018**, *11*, 3323−3334.
(13) Gawade, A. B.; Nakhate, A. V.; Yadav, G. D. Selective synthesis of 2, 5-furandicarboxylic acid by oxidation of 5-hydroxymethylfurfural over $MnFe_2O_4$ catalyst. *Catal. Today* **2018**, *309*, 119−125.
(14) Ventura, M.; Nocito, F.; de Giglio, E.; Cometa, S.; Altomare, A.; Dibenedetto, A. Tunable mixed oxides based on CeO_2 for the selective aerobic oxidation of 5-(hydroxymethyl)furfural to FDCA in water. *Green Chem.* **2018**, *20*, 3921−3926.
(15) Agarwal, B.; Kailasam, K.; Sangwan, R. S.; Elumalai, S. Traversing the history of solid catalysts for heterogeneous synthesis of 5-hydroxymethylfurfural from carbohydrate sugars: A review. *Renew. Sustain. Energy Rev.* **2018**, *82*, 2408−2425.
(16) Yamaguchi, Y.; Aono, R.; Hayashi, E.; Kamata, K.; Hara, M. Template-free synthesis of mesoporous β-MnO_2 nanoparticles: structure, formation mechanism, and catalytic properties. *ACS Appl. Mater. Interfaces* **2020**, *12*, 36004−36013.
(17) Chen, C.; Xu, K.; Ji, X.; Miao, L.; Jiang, J. Promoted electrochemical performance of beta-MnO_2 through surface engineering. *ACS Appl. Mater. Interfaces* **2017**, *9*, 15176−15181.
(18) Oxford, G. A. E.; Chaka, A. M. Structure and stability of hydrated β-MnO_2 surfaces. *J. Phys. Chem. C* **2012**, *116*, 11589−11605.
(19) Mellan, T. A.; Maenetja, K. P.; Ngoepe, P. E.; Woodley, S. M.; Catlow, C. R. A.; Grau-Crespo, R. Lithium and oxygen adsorption at the β-MnO_2 (110) surface. *J. Mater. Chem. A* **2013**, *1*, 14879.
(20) Tompsett, D. A.; Parker, S. C.; Islam, M. S. Rutile (beta-)MnO_2 surfaces and vacancy formation for high electrochemical and catalytic performance. *J. Am. Chem. Soc.* **2014**, *136*, 1418−1426.
(21) Chen; Xu, K.; Ji, X.; Miao, L.; Jiang, J. Promoted electrochemical performance of β-MnO_2 through surface engineering. *ACS Appl. Mater. Interfaces* **2017**, *9*, 15176−15181.
(22) Oxford, G. A. E.; Chaka, A. M. First-principles calculations of clean, oxidized, and reduced β-MnO_2 surfaces. *J. Phys. Chem. C* **2011**, *115*, 16992−17008.
(23) Posada, L. F.; Vil, A.; Perera, I. P.; March, S.; Suib, S. L. Oxygen vacancy-rich amorphous manganese oxide for the selective oxidation of 5-hydroxymethylfurfural. *ACS Appl. Energy Mater.* **2024**, *2*, 1816−1823.
(24) Yao, Y.-F.; Wang, G.-C. Mechanism insights into the aerobic oxidation of 5-hydroxymethylfurfural to 2,5-furandicarboxylic acid over MnO_2 catalysts. *J. Phys. Chem. C* **2021**, *125*, 3818−3826.
(25) de Oliveira, M. C.; Assis, M.; Simões, L. G. P.; Minozzi, D. T.; Ribeiro, R. A. P.; Andrés, J.; Longo, E. Unraveling the intrinsic biocidal activity of the SiO_2−Ag composite against SARS-CoV-2: A Joint Experimental and Theoretical Study. *ACS Appl. Mater. Interfaces* **2023**, *15*, 6548−6560.
(26) Lipsky, F.; Lacerda, L. H. d. S; Gracia, L.; Foschiani, B. G.; Assis, M.; Oliva, M.; Longo, E.; Andrés, J.; San-Miguel, M. A. A Tale of reactive oxygen species on the Ag_3PO_4(110). *Surface. J. Phys. Chem. C* **2023**, *127*, 23235−23245.
(27) Carvalho de Oliveira, M.; Longo, E.; Ribeiro, R. A. P.; Lemos, S. C. S.; Andrés, J.; Gracia, L. First-principles study on the stability, electronic structure, and band alignment of $AgNbO_3$ surfaces: Understanding the adsorption process of H_2O and O_2. *Comput. Mater. Sci.* **2025**, *246*, No. 113398.
(28) Hatakeyama, T.; Okamoto, N. L.; Ichitsubo, T. Thermal stability of MnO_2 polymorphs. *J. Solid State Chem.* **2022**, *305*, No. 122683.
(29) Kitchaev, D. A.; Dacek, S. T.; Sun, W.; Ceder, G. Thermodynamics of phase selection in MnO_2 framework structures through alkali intercalation and hydration. *J. Am. Chem. Soc.* **2017**, *139*, 2672−2681.
(30) Yuan, Y.; Liu, C.; Byles, B. W.; Yao, W.; Song, B.; Cheng, M.; Huang, Z.; Amine, K.; Pomerantseva, E.; Shahbazian-Yassar, R.; Lu, J. Ordering heterogeneity of [MnO_6] octahedra in tunnel-structured MnO_2 and its influence on ion storage. *Joule* **2019**, *3*, 471−484.
(31) Franchini, C.; Podloucky, R.; Paier, J.; Marsman, M.; Kresse, G. Ground-state properties of multivalent manganese oxides: Density functional and hybrid density functional calculations. *Phys. Rev. B* **2007**, *75*, No. 195128.
(32) Paik, Y.; Osegovic, J. P.; Wang, F.; Bowden, W.; Grey, C. P. 2H MAS NMR studies of the manganese dioxide tunnel structures and hydroxides used as cathode materials in primary batteries. *J. Am. Chem. Soc.* **2001**, *123*, 9367−9377.
(33) Kohn, W.; Sham, L. J. Self-consistent equations including exchange and correlation effects. *Phys. Rev.* **1965**, *140*, A1133−A1138.
(34) Kresse, G.; Furthmüller, J. Efficient iterative schemes for ab initio total-energy calculations using a plane-wave basis set. *Phys. Rev. B* **1996**, *54*, 11169−11186.
(35) Kresse, G.; Furthmüller, J. Efficiency of ab-initio total energy calculations for metals and semiconductors using a plane-wave basis set. *Comput. Mater. Sci.* **1996**, *6*, 15−50.
(36) Perdew, J. P.; Burke, K.; Ernzerhof, M. Generalized gradient approximation made simple. *Phys. Rev. Lett.* **1996**, *77*, 3865−3868.
(37) Blöchl, P. E. Projector augmented-wave method. *Phys. Rev. B* **1994**, *50*, 17953−17979.
(38) Kresse, G.; Joubert, D. From ultrasoft pseudopotentials to the projector augmented-wave method. *Phys. Rev. B* **1999**, *59*, 1758−1775.
(39) Liechtenstein, A. I.; Anisimov, V. I.; Zaanen, J. Density-functional theory and strong interactions: Orbital ordering in Mott-Hubbard insulators. *Phys. Rev. B* **1995**, *52*, R5467−R5470.
(40) Song, Z.; Yan, Z.; Yang, X.; Bai, H.; Duan, Y.; Yang, B.; Leng, L. First principles density functional theory study of Pb doped α-MnO_2 catalytic materials. *Chem. Phys. Lett.* **2018**, *695*, 216−221.
(41) Sato, H.; Wakiya, K.; Enoki, T.; Kiyama, T.; Wakabayashi, Y.; Nakao, H.; Murakami, Y. Magnetic structure of β-MnO_2 x-ray magnetic scattering study. *J. Phys. Soc. Jpn.* **2001**, *70*, 37−40.
(42) Grimme, S.; Antony, J.; Ehrlich, S.; Krieg, H. A consistent and accurate ab initio parametrization of density functional dispersion correction (DFT-D) for the 94 elements H-Pu. *J. Chem. Phys.* **2010**, *132*, 154104.
(43) Monkhorst, H. J.; Pack, J. D. Special points for Brillouin-zone integrations. *Phys. Rev. B* **1976**, *13*, 5188−5192.
(44) Smidstrup, S.; Pedersen, A.; Stokbro, K.; Jonsson, H. Improved initial guess for minimum energy path calculations. *J. Chem. Phys.* **2014**, *140*, 214106.
(45) Henkelman, G.; Jónsson, H. A dimer method for finding saddle points on high dimensional potential surfaces using only first derivatives. *J. Chem. Phys.* **1999**, *111*, 7010−7022.
(46) Henkelman, G.; Jónsson, H. Long time scale kinetic Monte Carlo simulations without lattice approximation and predefined event table. *J. Chem. Phys.* **2001**, *115*, 9657−9666.
(47) Olsen, R. A.; Kroes, G. J.; Henkelman, G.; Arnaldsson, A.; Jónsson, H. Comparison of methods for finding saddle points without knowledge of the final states. *J. Chem. Phys.* **2004**, *121*, 9776−9792.
(48) Kim, Y.; Cramer, C. J.; Truhlar, D. G. Steric effects and solvent effects on S_N2 reactions. *J. Phys. Chem. A* **2009**, *113*, 9109−9114.
(49) Regan, C. K.; Craig, S. L.; Brauman, J. I. Steric effects and solvent effects in ionic reactions. *Science* **2002**, *295*, 2245−2247.

https://doi.org/10.1021/acsomega.4c10253
ACS Omega 2025, 10, 12097−12108

(50) Garcia-Ratés, M.; López, N. Multigrid-based methodology for implicit solvation models in periodic DFT. *J. Chem. Theory Comput.* **2016**, *12*, 1331−1341.
(51) Zhang, Q.; Asthagiri, A. Solvation effects on DFT predictions of ORR activity on metal surfaces. *Catal. Today* **2019**, *323*, 35−43.
(52) Mathew, K.; Kolluru, V. S. C.; Mula, S.; Steinmann, S. N.; Hennig, R. G. Implicit self-consistent electrolyte model in plane-wave density-functional theory. *J. Chem. Phys.* **2019**, *151*, 234101.
(53) Tompsett, D. A.; Middlemiss, D. S.; Islam, M. S. Importance of anisotropic Coulomb interactions and exchange to the band gap and antiferromagnetism of β-MnO_2 from DFT+U. *Phys. Rev. B* **2012**, *86*, No. 205126.
(54) Gangwar, D.; Rath, C. Structural, optical and magnetic properties of α- and β-MnO_2 nanorods. *Appl. Surf. Sci.* **2021**, *557*, No. 149693.
(55) Andris, R.; Ridley, P.; Byles, B. W.; Cullen, D. A.; More, K. L.; Pomerantseva, E. Synthesis strategies toward improved ordering of $[MnO_6]$ octahedra in tunnel structured 2 × 3 and 2 × 4 MnO_2. *Scr. Mater.* **2021**, *195*, No. 113713.
(56) Housel, L. M.; Wang, L.; Abraham, A.; Huang, J.; Renderos, G. D.; Quilty, C. D.; Brady, A. B.; Marschilok, A. C.; Takeuchi, K. J.; Takeuchi, E. S. Investigation of α-MnO_2 tunneled structures as model cation hosts for energy storage. *Acc. Chem. Res.* **2018**, *51*, 575−582.
(57) Tompsett, D. A.; Parker, S. C.; Islam, M. S. Rutile β-MnO_2 surfaces and vacancy formation for high electrochemical and catalytic performance. *J. Am. Chem. Soc.* **2014**, *136* (4), 1418−1426.
(58) Nonneman, L. E. Y.; Ponec, V. Promotion and support effects in syngas reactions. *Catal. Lett.* **1991**, *7*, 197−203.
(59) Johnson, G. R.; Bell, A. T. Effects of Lewis acidity of metal oxide promoters on the activity and selectivity of Co-based Fischer−Tropsch synthesis catalysts. *J. Catal.* **2016**, *338*, 250−264.
(60) Tharat, B.; Ngamwongwan, L.; Seehamongkol, T.; Rungtaweevoranit, B.; Nonkumwong, J.; Suthirakun, S.; Faungnawakij, K.; Chanlek, N.; Plucksacholatarn, A.; Nimsaila, W.; Prommin, C.; Junkaew, A. Hydroxy and surface oxygen effects on 5-hydroxymethylfurfural oxidation to 2,5-furandicarboxylic acid on beta-MnO_2: DFT, microkinetic and experiment studies. *Nanoscale* **2024**, *16*, 678−690.
(61) Chen, C.-T.; Nguyen, C. V.; Wang, Z.-Y.; Bando, Y.; Yamauchi, Y.; Bazziz, M. T. S.; Fatehmulla, A.; Farooq, W. A.; Yoshikawa, T.; Masuda, T.; Wu, K. C.-W. Hydrogen peroxide assisted selective oxidation of 5-hydroxymethylfurfural in water under mild conditions. *ChemCatChem.* **2018**, *10*, 361−365.
(62) Gupta, S. S. R.; Vinu, A.; Kantam, M. L. Copper-catalyzed oxidative methyl-esterification of 5-hydroxymethylfurfural using TBHP as an oxidizing and methylating reagent: A new approach for the synthesis of furan-2,5-dimethylcarboxylate. *J. Catal.* **2020**, *389*, 259−269.
(63) Wang, Y.; Yu, L.; Zhang, F.; Chen, Q.; Zhan, Y.; Meng, L.; Zheng, X.; Wang, H.; Qin, Z.; Qin, G. The consistent behavior of negative Poisson's ratio with interlayer interactions. *Adv. Mater.* **2022**, *3*, 4334−4341.
(64) Xiao, G.; Lu, R.; Liu, J.; Liao, X.; Wang, Z.; Zhao, Y. Coordination environments tune the activity of oxygen catalysis on single atom catalysts: A computational study. *Nano Research* **2022**, *15*, 3073−3081.
(65) Zhang, S.; Huang, Z. Q.; Ma, Y.; Gao, W.; Li, J.; Cao, F.; Li, L.; Chang, C. R.; Qu, Y. Solid frustrated-Lewis-pair catalysts constructed by regulations on surface defects of porous nanorods of CeO_2. *Nat. Commun.* **2017**, *8*, 15266.
(66) Stephan, D. W. Frustrated Lewis pairs: from concept to catalysis. *Acc. Chem. Res.* **2015**, *48*, 306−316.
(67) Huang, Z.-Q.; Liu, L.-P.; Qi, S.; Zhang, S.; Qu, Y.; Chang, C.-R. Understanding all-solid frustrated-lewis-pair sites on CeO_2 from theoretical perspectives. *ACS Catal.* **2018**, *8*, 546−554.
(68) Xu, X.; Wang, C.; Fronzi, M.; Liu, X.; Bi, L.; Zhao, X. S. Modification of a first-generation solid oxide fuel cell cathode with Co_3O_4 nanocubes having selectively exposed crystal planes. *J. Renewable Sustainable Energy* **2019**, *8*, 15.
(69) Zhang, J.; Zhang, D.-M. First-principles study of oxygen adsorbed on Au-doped RuO_2 (110) surface*. *Chin. Phys. B* **2019**, *28*, 116107.
(70) Wang, Y.; Li, Y.; Lu, Z.; Wang, W. Improvement of O_2 adsorption for α-MnO_2 as an oxygen reduction catalyst by Zr^{4+} doping. *RSC Adv.* **2018**, *8*, 2963−2970.
(71) Xu, X.; Zhang, Y.; Chen, Y.; Liu, C.; Wang, W.; Wang, J.; Huang, H.; Feng, J.; Li, Z.; Zou, Z. Revealing *OOH key intermediates and regulating H_2O_2 photoactivation by surface relaxation of Fenton-like catalysts. *Proc. Natl. Acad. Sci. U. S. A.* **2022**, *119*, No. e2205562119.
(72) Lin, P. J.; Yeh, C. H.; Jiang, J. C. Theoretical insight into hydroxyl production via H_2O_2 decomposition over the Fe_3O_4(311) surface. *RSC Adv.* **2021**, *11*, 36257−36264.
(73) Reuter, K. Ab initiothermodynamics and first-principles microkinetics for surface catalysis. *Catal. Lett.* **2016**, *146*, 541−563.
(74) Chaka, A. M.; Felmy, A. R. Ab initio thermodynamic model for magnesium carbonates and hydrates. *J. Phys. Chem. A* **2014**, *118*, 7469−7488.
(75) Reuter, K.; Stampf, C.; Scheffler, M., AB initio atomistic thermodynamics and statistical mechanics of surface properties and functions. In *Handbook of Materials Modeling: Methods*; Yip, S., Ed.; Springer Netherlands: Dordrecht, 2005; pp 149−194.
(76) Reuter, K.; Scheffler, M. First-principles atomistic thermodynamics for oxidation catalysis: surface phase diagrams and catalytically interesting regions. *Phys. Rev. Lett.* **2003**, *90*, No. 046103.
(77) Li, B.; Guinness, S. M.; Hoagland, S.; Fichtner, M.; Kim, H.; Li, S.; Maguire, R. J.; McWilliams, J. C.; Mustakis, J.; Raggon, J.; Campos, D.; Voss, C. R.; Sohodski, E.; Feyock, B.; Murnen, H.; Gonzalez, M.; Johnson, M.; Lu, J.; Feng, X.; Sun, X.; Zheng, S.; Wu, B. Continuous production of anhydrous tert-butyl hydroperoxide in nonane using membrane pervaporation and its application in flow oxidation of a γ-butyrolactam. *Org. Process Res. Dev.* **2018**, *22*, 707−720.

https://doi.org/10.1021/acsomega.4c10253
ACS Omega 2025, 10, 12097−12108